catalysts

MDPI

Article

Study on the Catalytic Activity and Selectivity of Manganese Dioxide-Modified Nickel–Iron-Based Hydroxide Electrodes for Initiating the Oxygen Evolution Reaction in Natural Seawater

Fangfang Liu [1], Miaomiao Fan [2], Haofeng Yan [2], Zheng Wang [2], Jimei Song [1], Hui Wang [2,*] and Jianwei Ren [3,*]

[1] Shandong Engineering Laboratory for Clean Utilization of Chemical Resources, Shandong Peninsula Blue Economy and Engineering Research Institute, Weifang University of Science and Technology, Shouguang 262700, China
[2] College of Chemical Engineering, Qingdao University of Science and Technology, Qingdao 266042, China
[3] Department of Chemical Engineering, University of Pretoria, Hatfield, Pretoria 0028, South Africa
* Correspondence: wangh@qust.edu.cn (H.W.); jianwei.ren@up.ac.za (J.R.)

Abstract: Transition metal oxides, particularly $NiFe(OH)_2$, are recognized for their high oxygen evolution reaction (OER) activity and structural stability. However, their performance in natural seawater electrolysis remains insufficiently studied. Manganese dioxide (MnO_2), which is known for its multiple crystal phases and high OER selectivity, can be incorporated to enhance the catalytic properties. In this study, the OER catalytic performance of carbon cloth-supported manganese dioxide-modified nickel–iron bimetallic hydroxide (MnO_2-NiFe-LDH/CC) electrodes was explored in both alkaline and natural seawater. Electrochemical tests demonstrated that the MnO_2-NiFe-LDH/CC electrode achieved overpotentials of 284 mV and 363 mV at current densities of 10 $mA{\cdot}cm^{-2}$ and 100 $mA{\cdot}cm^{-2}$, respectively, with a Tafel slope of 68.6 $mV{\cdot}dec^{-1}$ in alkaline seawater. Most importantly, the prepared MnO_2-NiFe-LDH/CC electrode maintained stable OER performance over 120 h of testing. In natural seawater, the MnO_2-NiFe-LDH/CC electrode outperformed the NiFe-LDH/CC electrode by exhibiting an oxygen evolution selectivity of 61.1%. This study highlights the potential of MnO_2-modified nickel–iron-based materials for efficient and stable OER in seawater electrolysis, which offers a promising approach for sustainable hydrogen production in coastal desert regions.

Keywords: catalytic activity and selectivity; manganese dioxide; nickel–iron-based hydroxide electrodes; oxygen evolution reaction; natural seawater

Citation: Liu, F.; Fan, M.; Yan, H.; Wang, Z.; Song, J.; Wang, H.; Ren, J. Study on the Catalytic Activity and Selectivity of Manganese Dioxide-Modified Nickel–Iron-Based Hydroxide Electrodes for Initiating the Oxygen Evolution Reaction in Natural Seawater. *Catalysts* **2024**, *14*, 502. https://doi.org/10.3390/catal14080502

Academic Editor: Nicolas Alonso-Vante

Received: 27 June 2024
Revised: 30 July 2024
Accepted: 31 July 2024
Published: 2 August 2024

1. Introduction

Hydrogen is not only a carbon-free energy carrier with extremely high energy density but also a crucial raw material for hydrogenation, petroleum refining, and fertilizer production [1]. Hydrogen production through seawater electrolysis is a viable option, especially in coastal desert regions like the Middle East, where freshwater resources are scarce [2]. By effectively substituting seawater for freshwater in various applications, the freshwater scarcity crisis can be alleviated to some extent. Seawater electrolysis technology is also environmentally friendly and easy to operate [3]. However, the generation of oxygen is often inhibited because seawater contains chloride ions, which lead to the production of chlorine gas at the anode during electrolysis. The release of chlorine gas poses serious health risks, corrodes equipment, and causes environmental pollution [4]. Therefore, developing anode materials that promote oxygen evolution while suppressing chlorine evolution is crucial for clean hydrogen production from seawater electrolysis technology [5]. In the literature, noble metal oxides are reported as the benchmark anode catalysts for the oxygen evolution reaction (OER), due to their rapid reaction kinetics [6,7]. However, the high costs of these noble metal catalysts remain major obstacles to their practical application [8,9]. Although some non-noble metal electrocatalysts, including metal oxides, metal nitrides

and oxynitrides [10], metal carbides and carbonitrides [11], metal sulfides [12], and hydroxides [13], have also been reported with good catalytic performance in catalyzing the OER in seawater electrolysis, it should be noted that the seawater used in these studies was usually simulated seawater or alkaline seawater. Typically, simulated seawater contains only a strong alkali and NaCl, while alkaline seawater is natural seawater with a certain amount of KOH or NaOH present. Compared to natural seawater, simulated seawater has a simpler composition, and the performance of electrodes in simulated seawater significantly differs from that in natural seawater. More specifically, the concentration of OH^- in alkaline seawater is much higher than that in natural seawater, which greatly accelerates the OER kinetics in alkaline seawater and suppresses the chlorine evolution process. Therefore, using simulated seawater or alkaline seawater to draw analogies about the performance of anodes in natural seawater is incomplete for effective seawater electrolysis research.

In this study, the performance of carbon cloth-supported manganese dioxide-modified nickel–iron bimetallic hydroxide electrodes was investigated for catalyzing the OER in natural seawater. The focus was on both the catalytic activity of the electrodes in promoting OER and their selectivity toward oxygen evolution under natural seawater conditions. As is well-known, transition metal oxides are a class of positively charged oxides valued for their rich catalytic sites, structural stability, environmental friendliness, and ease of synthesis. Through methods such as controlling the metal atom ratio [14], adjusting defects in the crystal structure [15], modifying the crystalline phase of $NiFe(OH)_2$ [16,17], and changing the substrate material [18], $NiFe(OH)_2$, as one of the best and most recognized OER catalysts, has achieved an alkaline OER potential of 1.45 V vs. RHE and a current density of 100 mA/cm^2 [19]. In a previous study by Dionigi et al. [20], $NiFe(OH)_2$ exhibited good OER catalytic activity and 100% selectivity in artificial seawater or alkaline solutions with NaCl, even with the presence of chloride ions. However, it is still necessary to verify whether $NiFe(OH)_2$ can be effectively applied as an anode catalyst in natural seawater electrolysis. Meanwhile, manganese dioxide (MnO_2) has been reported as having high catalytic activity and selectivity for the OER in seawater electrolysis. This is attributed to its multiple crystal phases and morphologies, which are generated by various tunnel structures from [MnO_6] structural units with different stacking and connecting styles [21–23]. For instance, Sang et al. [24] studied the activity and oxygen evolution selectivity of γ-MnO_2 and its electrodes when doped with different elements. They achieved 100% oxygen evolution selectivity after optimization. However, their electrode consisted of a titanium plate + IrO_2 substrate, which indicated a collective catalytic performance of IrO_2 and γ-MnO_2. Similar structures were also reported by Vos et al. [25], which further emphasized the positive effect of MnO_2 as an additive component in seawater electrolysis anode catalysts.

In this work, considering the inertness of carbon cloth (CC) substrate toward Cl_2 and ClO^-, a manganese dioxide-modified nickel–iron hydroxide electrode catalyst (MnO_2-NiFe-LDH) was constructed into a three-dimensional (3D) self-supporting electrode, using CC as the substrate (MnO_2-NiFe-LDH/CC). Their catalytic activity and selectivity for oxygen evolution in natural seawater electrolysis were investigated. The results showed that the optimal MnO_2-NiFe-LDH/CC electrode sample exhibited an excellent OER catalytic performance in seawater electrolysis, with an oxygen evolution selectivity of 61.1%.

2. Results and Discussion

Figure S1 in the Supplementary Materials illustrates the preparation procedure of the 3D MnO_2-NiFe-LDH/CC electrode sample. First, NiFe-LDH nanosheet arrays were grown on the surface of pure CC, followed by the hydrothermal growth of MnO_2 on the NiFe-LDH surface. For optimization, the amount of the precursor $KMnO_4$ was adjusted to produce electrode samples with different MnO_2 loadings, which were then electrochemically tested in 1.0 M KOH for screening. As shown in Figure S2a, the MnO_2-NiFe-LDH/CC-0.01 mmol electrode sample exhibited the lowest voltage and the lowest onset potential at the same current density (100 $mA{\cdot}cm^{-2}$), which indicates that the electrocatalyst with this MnO_2 loading achieved the highest OER catalytic activity. The bar chart in Figure S2b presents the

exact overpotential values of four electrode samples with different MnO_2 loadings at current densities of 50 $mA \cdot cm^{-2}$ and 100 $mA \cdot cm^{-2}$, respectively. As illustrated, the MnO_2-NiFe-LDH/CC-0.01 mmol electrode sample presents the lowest oxygen evolution overpotential. As shown in Figure S2c, the kinetic performance of the MnO_2-NiFe-LDH/CC electrode sample was investigated using the Tafel slope, and the MnO_2-NiFe-LDH/CC-0.01 mmol sample exhibited a lower Tafel slope of 68.6 $mV \cdot dec^{-1}$. This result aligns with the analysis of the LSV curves in confirming that the MnO_2-NiFe-LDH/CC-0.01 mmol electrode sample exhibited the best OER catalytic activity among the six catalytic samples. The mass change of the samples before and after MnO_2 loading was recorded to calculate the MnO_2 loading value. The MnO_2 loading in the MnO_2-NiFe-LDH/CC-0.01 mmol electrode with the best OER performance was 0.54 $mg \cdot cm^{-2}$. Therefore, subsequent discussions will refer exclusively to the optimal MnO_2-NiFe-LDH/CC sample. For convenience, this optimal sample will be referred to simply as MnO_2-NiFe-LDH/CC.

Figure 1a–c depicts the scanning electron microscope (SEM) images of the NiFe-LDH/CC sample, wherein NiFe-LDH was hydrothermally deposited on the surface of the CC substrate. In Figure 1a, the NiFe-LDH/CC sample shows intertwined fluffy carbon fibers with diameters of around 6 µm. By comparison with the SEM images of CC carbon fibers in Figure S3 in the Supplementary Materials, it is evident that the fluffy material on the NiFe-LDH/CC fibers' surface is a NiFe-LDH species, and the carbon fiber surfaces are uniform and well-structured. This uniformity indicates an even distribution of NiFe-LDH on the CC surface. The magnified images in Figure 1b,c reveal that NiFe-LDH consists of interwoven sheets with relatively smooth surfaces. This interconnected nanosheet structure is beneficial as it exposes a larger specific surface area. Figure 1d–f shows SEM images of the MnO_2-NiFe-LDH/CC sample. Compared to Figure 1a, Figure 1d displays aggregated clusters of heterogeneous MnO_2 clusters on the fiber surface. Upon magnification, these MnO_2 clusters resemble willow catkins, as seen in Figure 1e. Zooming into the uniformly covered parts of the fibers (indicated by the red box) still reveals interwoven sheets on the carbon fiber surface. However, comparing Figure 1c,f shows that the sheets in Figure 1f appear bent. Based on previous research [26], these bent sheets in Figure 1f can be identified as interlinked MnO_2 sheet layers that are deposited on top of the NiFe-LDH layer.

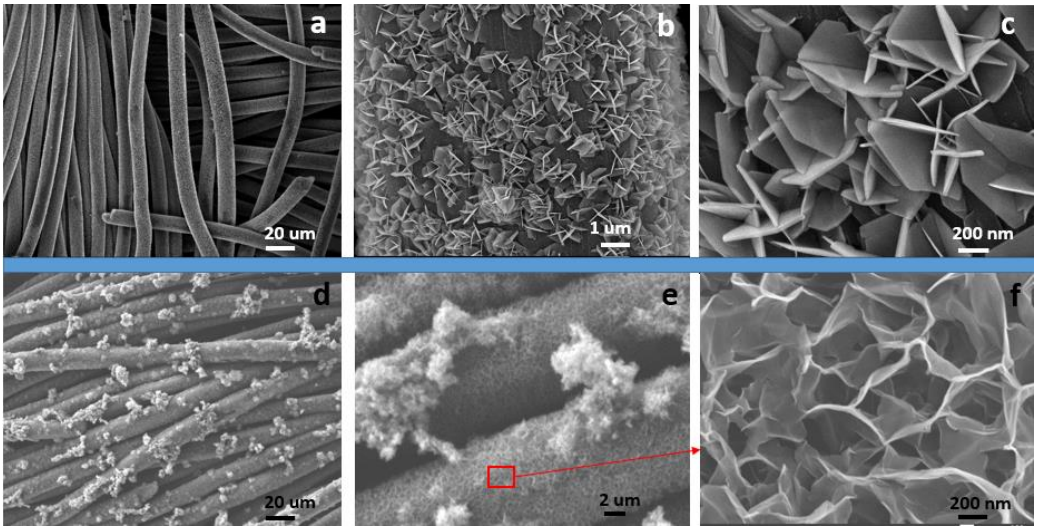

Figure 1. SEM images at different magnifications of samples: (**a**–**c**) NiFe-LDH/CC and (**d**–**f**) MnO_2-NiFe-LDH/CC.

Figure 2a,b presents the X-ray diffraction (XRD) spectra of the prepared samples. In the NiFe-LDH/CC spectrum (Figure 2a), the diffraction peaks observed at 2θ values of 11.4°, 22.9°, 33.5°, 34.4°, 59.9°, and 61.3° correspond to the (003), (006), (101), (012), (110), and (113) crystal planes, respectively. These peaks match the standard XRD pattern (PDF#40-

0215) for NiFe-LDH. In the XRD spectrum of the MnO_2-NiFe-LDH/CC sample (Figure 2b), in addition to the standard NiFe-LDH/CC diffraction peaks, three additional peaks are observed at 2θ values of 12.54°, 25.24°, and 36.22°. These peaks can be attributed to the characteristic peaks of the δ-phase MnO_2 (PDF#80-1098), which indicates that the MnO_2 grown on the CC substrate is in the δ-phase [27–29]. The fine structure of the obtained samples was further characterized using transmission electron microscopy (TEM). The samples were prepared by ultrasonic separation from the nickel foam substrate. The TEM image in Figure S4 in the Supplementary Materials reveals the relatively thin sheets of the NiFe-LDH sample. The high-resolution TEM image displays lattice fringes with a spacing of 0.25 nm, which corresponds to the (012) plane of NiFe-LDH. The TEM image in Figure 2c shows sheet-like structures in the MnO_2-NiFe-LDH/CC sample over a large area. Enlarged images of the different areas (Figure 2d,e) reveal a lighter color contrast; this indicates relatively thin sheets, which is consistent with the SEM observations. At higher magnification (Figure 2f), some regions of these sheets exhibit high crystallinity, with long lattice fringes observed in the left region that likely originate from the NiFe-LDH. Other areas lacking clear lattice fringes suggest lower crystallinity, which corresponds to MnO_2 sheet structures, based on XRD analysis. This mixed crystalline structure is further supported by the multiple concentric rings observed in the selected area electron diffraction (SAED) pattern (Figure 2g). With the selected area shown in Figure 2h_1, the elemental mapping of the MnO_2-NiFe-LDH/CC sample in Figure 2h_2–h_5 confirms the uniform distribution of Ni, Fe, Mn, and O elements. This demonstrates the homogeneous distribution of all four elements within the MnO_2-NiFe-LDH/CC sample and affirms the uniform structure of the sheets observed in Figure 2c.

X-ray photoelectron spectroscopy (XPS) was employed to analyze the elemental composition and surface chemical states of the MnO_2-NiFe-LDH/CC-0.01 mmol sample (Figure 3). The high-resolution XPS spectrum of Ni 2p (Figure 3a) exhibits characteristic peaks at binding energies of 855.5 eV and 873.4 eV. These correspond to Ni $2p_{3/2}$ and Ni $2p_{1/2}$, respectively, and imply the presence of the Ni^{2+} oxidation state. Two peaks are observed in the Fe 2p XPS spectrum (Figure 3b) at binding energies of 711.6 eV and 723.6 eV, which typify Fe $2p_{3/2}$ and Fe $2p_{1/2}$, respectively, and indicate the presence of trivalent iron (Fe^{3+}) [30–32]. In the Mn 2p XPS spectrum (Figure 3c), the two peaks at 642 eV and 654 eV are attributable to Mn $2p_{3/2}$ and Mn $2p_{1/2}$, respectively. After convolution fitting of the spin-orbit peaks, four peaks corresponding to the Mn^{3+} and Mn^{4+} oxidation states are obtained. The peaks at 642.3 eV and 653.8 eV are associated with Mn^{3+}, while the peaks at 644.0 eV and 655.5 eV are associated with Mn^{4+}. By comparing the peak areas, it is evident that the area for Mn^{3+} is larger than that for Mn^{4+}, which implies that the Mn is predominantly in the +3-oxidation state. The O 1s spectrum in Figure 3d can be deconvoluted into three peaks corresponding to interlayer oxygen (Mn-O-Mn), adsorbed hydroxyl groups (Mn-OH), and possibly bound water (–H_2O) [33].

The OER performance of the prepared MnO_2-NiFe-LDH/CC-0.01 mmol electrode and the comparative samples was evaluated in a 1.0 M KOH solution. Figure S7a in the Supplementary Materials displays the linear sweep voltammetry (LSV) curves at a scan rate of 5 mV/s, which were measured after multiple cyclic voltammetry (CV) scans to ensure reproducibility. It was observed that the NiFe-LDH/CC sample exhibited the lowest onset potential, and, thus, the highest OER activity among the tested samples. The catalytic performance of the MnO_2-NiFe-LDH/CC-0.01 mmol sample for OER was slightly lower than that of the NiFe-LDH/CC sample, which is due to the poor conductivity of the MnO_2 loaded on the surface of NiFe-LDH/CC. Figure S7b presents the overpotential of different catalysts at various current densities. The overpotentials for the MnO_2-NiFe-LDH/CC-0.01 mmol composite electrode at current densities of 10 $mA \cdot cm^{-2}$ and 100 $mA \cdot cm^{-2}$ were 284 mV and 363 mV, respectively. The Tafel slope in Figure S7c was obtained by fitting the corresponding LSV curves in Figure S7a and was used to evaluate the reaction kinetics of the catalytic samples [34–36]. The Tafel slope for the MnO_2-NiFe-LDH/CC-0.01 mmol electrode sample (68.6 $mV \cdot dec^{-1}$) was slightly lower than that of the NiFe-LDH/CC

sample, which is consistent with the previously observed trend. Due to poor current response signals from the MnO_2 and the pure CC substrate, their data were not included in the overpotential bar chart and Tafel slope plot. The charge transfer resistance (R_{ct}) reflects the kinetics of the OER for the catalyst. Impedance tests were performed at a voltage of 1.48 V (vs. RHE). Figure S7d reveals that the semicircle for the NiFe-LDH/CC sample is the smallest, followed by that of the MnO_2-NiFe-LDH/CC-0.01 mmol sample. This indicates that NiFe-LDH/CC has the lowest impedance value; therefore, it correlates with the best OER catalytic performance. This is consistent with the results from the LSV curve analysis. Figure S7e demonstrates the constant current stability of the MnO_2-NiFe-LDH/CC-0.01 mmol sample in alkaline seawater. The potential remained stable during 100 h of continuous electrolysis. Figure S7f compares the LSV curves of the electrode material before and after 6000 cycles of CV testing. The slight potential shift of 8 mV to the right suggests that the catalyst maintained long-term stability in alkaline seawater, further demonstrating its durability and effectiveness.

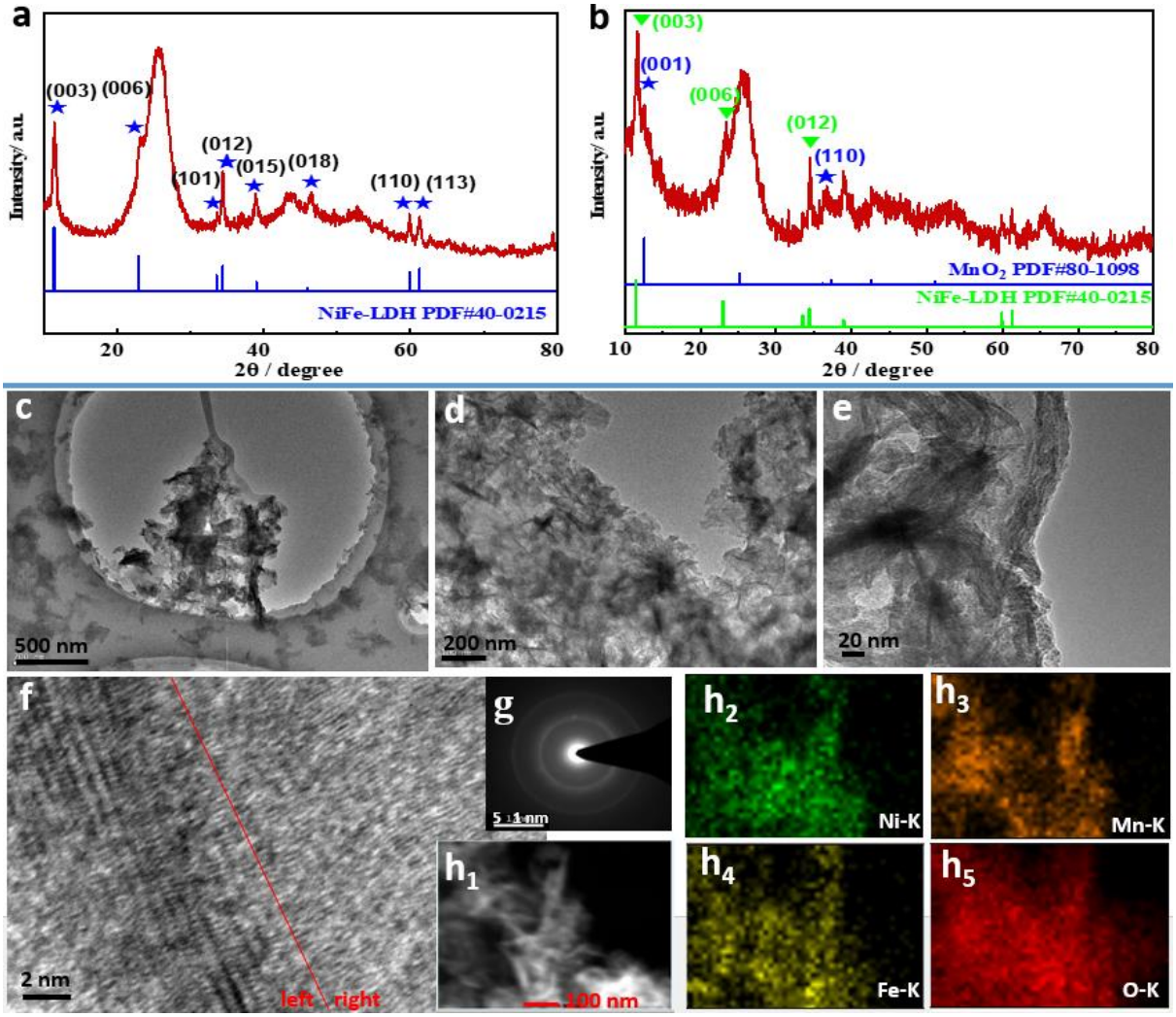

Figure 2. XRD patterns of the samples: (**a**) NiFe-LDH/CC and (**b**) MnO_2-NiFe-LDH/CC. (**c**–**f**) TEM images at different magnifications, (**g**) SAED, ($\mathbf{h_1}$) STEM, and ($\mathbf{h_2}$–$\mathbf{h_5}$) elemental mapping of the MnO_2-NiFe-LDH/CC sample.

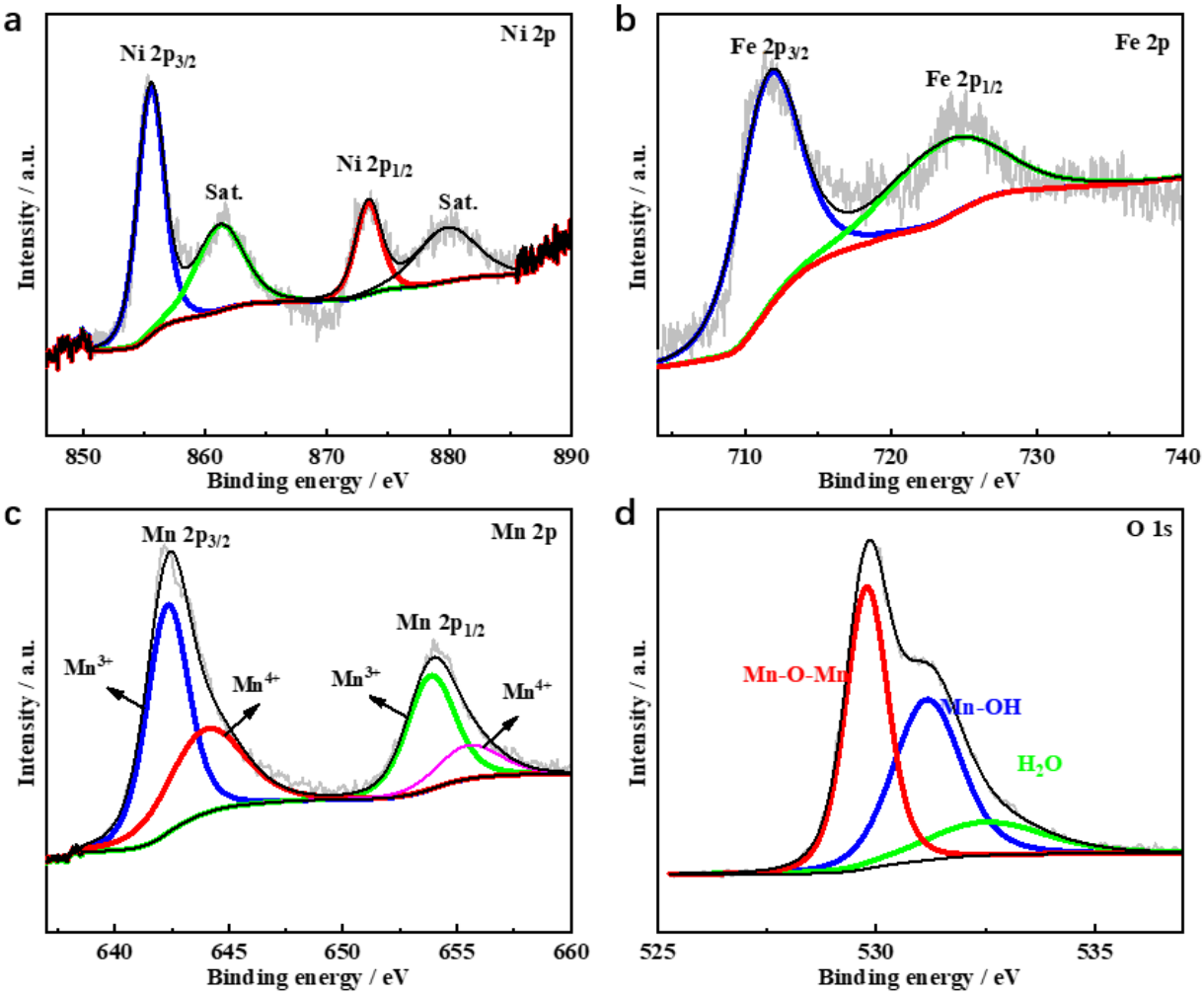

Figure 3. The high-resolution XPS spectra of MnO_2-NiFe-LDH/CC-0.01 mmol sample: (**a**) Ni 2p, (**b**) Fe 2p, (**c**) Mn 2p, and (**d**) O 1s.

The electrochemical active surface area (ECSA) of the different catalyst samples was evaluated through double-layer capacitance (C_{dl}) measurements. CV tests were conducted at various scan rates (20 mV/s, 40 mV/s, 60 mV/s, 80 mV/s, 100 mV/s, and 120 mV/s) in the non-Faradaic region (0.924–1.024 V vs. RHE). Figure S8a–c shows the CV curves of the CC, MnO_2/CC, NiFe-LDH/CC, and MnO_2-NiFe-LDH/CC-0.01 mmol samples at different scan rates. Figure S8d was obtained after plotting the difference in current density against the scan rate and fitting the data. As can be seen, the C_{dl} value for MnO_2-NiFe-LDH/CC-0.01 mmol is 1.74 mF·cm^{-2}, which is lower than the C_{dl} value of the NiFe-LDH/CC sample (2.38 mF·cm^{-2}). The ECSA is proportional to the C_{dl} and a higher C_{dl} value indicates a larger electrochemical active area, with more active sites exposed on the catalyst sample [37]. The surface loading of MnO_2 on NiFe-LDH/CC results in the coverage of its active sites and leads to a decrease in the catalytic performance of the OER.

Using natural seawater as the electrolyte, the OER catalytic performance of the prepared electrode samples was studied. Initially, CV scans were performed at a scan rate of 50 mV/s within a potential window from −1 V to 0.2 V to activate the electrode samples. After ensuring the complete overlap of the CV curves, LSV tests were conducted to assess the OER performance under natural seawater conditions (Figure 4). At this point, the sample had been activated in an equilibrium state and was capable of truly reflecting the OER's catalytic performance in the LSV test. As shown in Figure 4a, the LSV tests were conducted at a scan rate of 5 mV/s, using MnO_2-NiFe-LDH/CC-0.01 mmol and comparative samples in natural seawater electrolytes. It can be observed that the pure CC

substrate and MnO_2/CC sample exhibited significantly weaker current response signals compared to those from the MnO_2-NiFe-LDH/CC-0.01 mmol and NiFe-LDH/CC samples. More specifically, the MnO_2-NiFe-LDH/CC-0.01 mmol sample showed the lowest onset potential and overpotential out of the four samples, which indicates the superior activity of the OER in seawater electrolytes. The OER performance of the NiFe-LDH/CC sample in seawater was weaker than that of the MnO_2-NiFe-LDH/CC-0.01 mmol sample. This performance contrasts with that observed in alkaline seawater. The reason for this may lie in the fact that during the electrolysis of seawater, the amount of charge available for Cl^- oxidation by the NiFe-LDH/CC sample is higher than that for Cl^- oxidation by the MnO_2-NiFe-LDH/CC-0.01 mmol sample. The Tafel slopes in Figure 4b were obtained by fitting the LSV curve data. They reveal that the MnO_2-NiFe-LDH/CC-0.01 mmol sample has the smallest Tafel slope value of 421.4 mV/dec, which is significantly higher than the Tafel slope obtained in alkaline seawater. This difference is primarily due to the enhanced kinetics of the OER reaction in strong alkaline electrolytes, where the pH is approximately 14, whereas natural seawater has a pH of around 8. Additionally, in mildly alkaline natural seawater, the presence of abundant Cl^- ions leads to chlorine evolution reactions at the anode, and the chlorine gas thus produced may corrode the electrode materials, thereby reducing their OER performance. Figure 4c–f shows the chronoamperometry plots recorded for the CC, MnO_2/CC, NiFe-LDH/CC, and MnO_2-NiFe-LDH/CC-0.01 mmol samples during constant current electrolysis experiments. The inset images demonstrate that the tested samples can recover their original shape after any deformation caused by external forces.

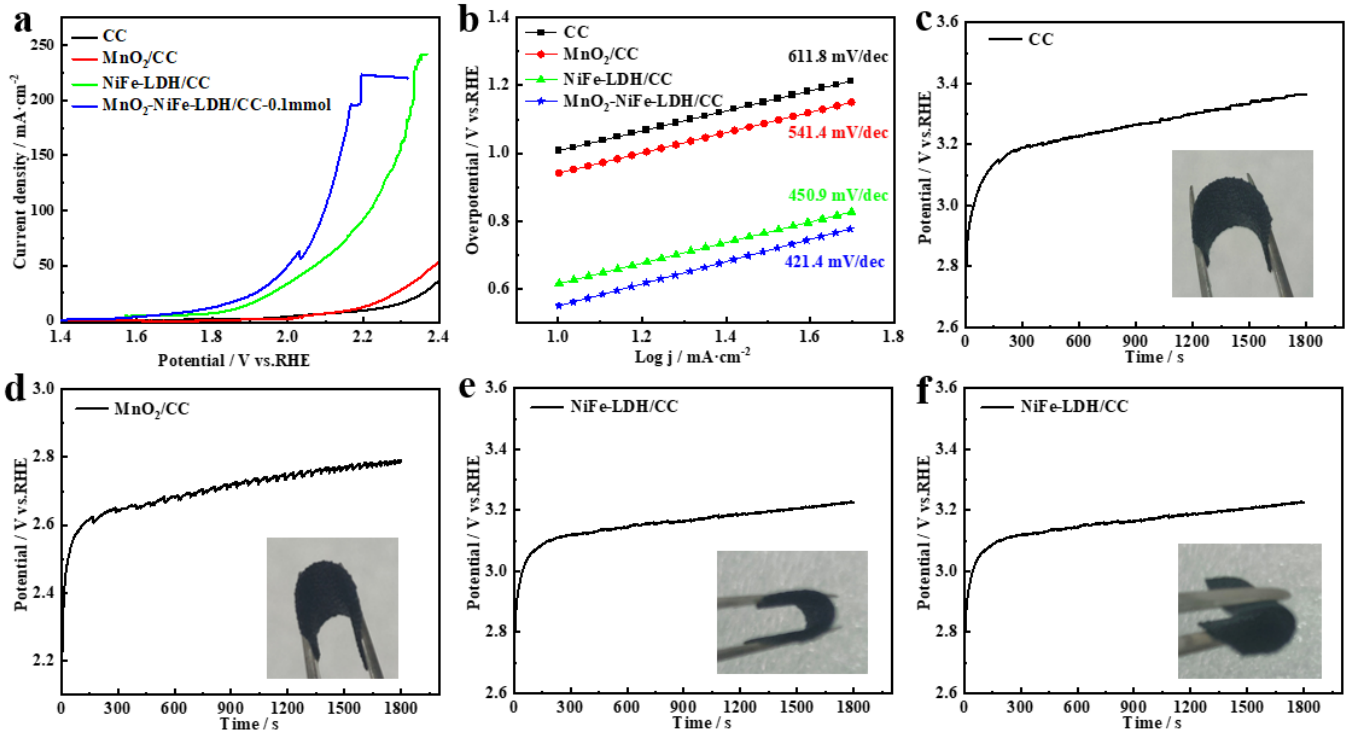

Figure 4. (**a**) OER LSV of CC, MnO_2/CC, NiFe-LDH/CC, and MnO_2-NiFe-LDH/CC-0.01 mmol electrode samples in seawater at a scan rate of 5 mV/s. (**b**) Tafel plots. Constant current curve of samples: (**c**) CC, (**d**) MnO_2/CC, (**e**) NiFe-LDH/CC, and (**f**) MnO_2-NiFe-LDH/CC-0.01 mmol electrode at a current of 0.1 A.

After constant current electrolysis, titration was conducted on both the anodic and absorptive solutions; the color changes during titration are illustrated in Figure S9a–e in the Supplementary Materials. Upon adding KI solution, the solution turned yellow-brown, and with the addition of $Na_2S_2O_3$, the solution gradually lightened. The solution in Figure S9d turned blue because a starch solution was added. The purpose of this addition is to make the color change more noticeable as it approaches the titration endpoint. Figure S9f shows images of the cathodic and anodic regions during constant current electrolysis under seawater electrolyte conditions. In the cathodic region, there was a noticeable formation of white flocculent and precipitate due to the hydrogen evolution reaction ($2H_2O + 2e^- \rightarrow 2OH^- + H_2$), wherein OH^- ions reacted with the Ca^{2+} and Mg^{2+} ions present in seawater to form precipitates. Before conducting the experiment, it is crucial to ensure that the setup is well-sealed. A tube connected the anodic region to the Cl_2 absorption device, as shown in Figure S9g. Cl_2 gas produced at the anode reacts with NaOH in the absorption device ($2NaOH + Cl_2 = NaCl + NaClO + H_2O$) and results in the formation of ClO^-. By recording the volume of $Na_2S_2O_3$ solution consumed during the titration, the amount of charge required for the oxidation of Cl^- to Cl_2 in the anode solution can be calculated. Similarly, titration of the anodic solution is necessary to determine the amount of charge required for the oxidation of Cl^- to ClO^- in the anode solution. By combining the titration results of the Cl_2 absorption solution and the anodic solution, the total charge consumed during electrolysis and the charge used for Cl oxidation can be determined. The ratio of the charge consumed for oxygen evolution to the total charge during constant current electrolysis gives the oxygen evolution selectivity.

During the titration process, the volumes of $Na_2S_2O_3$ solution consumed in the anodic region and the Cl_2 absorption region were recorded, as depicted in Figure 5a. The MnO_2-modified NiFe-LDH/CC sample consumed less $Na_2S_2O_3$ solution volume compared to its precursor. Figure 5b–e shows the proportions of OER and chlorine evolution reaction (ClER) for the four electrode samples in natural seawater, while Figure 5f presents the oxygen evolution selectivity of these samples. Experimental data indicated that the composite MnO_2-NiFe-LDH/CC-0.01 mmol electrode sample exhibited an oxygen evolution selectivity of 61.1% in natural seawater, which was approximately 10% higher than the NiFe-LDH/CC sample. As shown in Figure S10, the presence of MnO_2 in the MnO_2-NiFe-LDH/CC sample enhanced the OH^- adsorption capacity and reduced the Cl^- adsorption capacity compared to the NiFe-LDH/CC sample. This led to increased oxygen generation and improved oxygen evolution selectivity. This suggests that in natural seawater, the actual OER efficiency of the MnO_2-NiFe-LDH/CC-0.01 mmol sample was greater than that of the NiFe-LDH/CC sample. The variation in OER performance between alkaline seawater and natural seawater electrolytes can be attributed to the different oxygen evolution selectivity of these two samples. Moreover, the higher oxygen evolution selectivity of the MnO_2/CC sample compared to pure CC substrate indicates that loading δ-MnO_2 is beneficial for catalytic materials that are used in natural seawater electrolysis conditions.

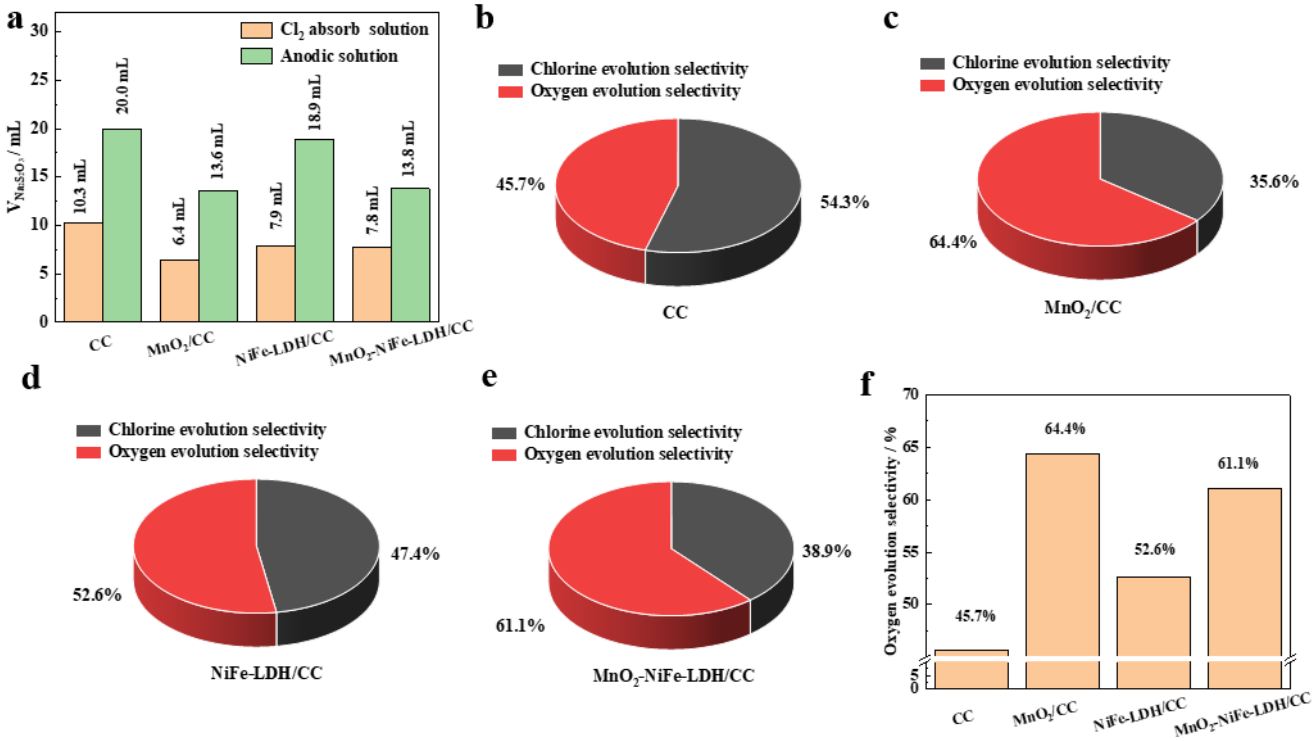

Figure 5. (**a**) The electrode material consumes a volume of $Na_2S_2O_3$ during titration. The ratios of oxygen and chlorine evolution in electric natural seawater samples: (**b**) CC, (**c**) MnO_2/CC, (**d**) NiFe-LDH/CC, and (**e**) MnO_2-NiFe-LDH/CC electrode samples. (**f**) Oxygen evolution selectivity of the electrode materials in natural seawater.

3. Experiments

3.1. Preparation of the NiFe-LDH/CC Sample

Typically, 0.66 mmol of $Ni(NO_3)_2{\cdot}6H_2O$, 0.33 mmol of $Fe(NO_3)_3{\cdot}9H_2O$, 2 mmol of NH_4F, and 5 mmol of $CO(NH_2)_2$ were dissolved in 25 mL of deionized water. The mixture was stirred for 10 min before being transferred to a reactor. Then, a piece of pre-treated CC with dimensions of 2 × 3 cm^2 was added. Subsequently, the reactor was heated up to 120 °C and maintained at that temperature for 6 h. Afterward, the sample was collected and washed ultrasonically to remove any yellow-green precipitate on the surface. Lastly, the sample was dried in a vacuum oven at 60 °C and labeled as NiFe-LDH/CC.

3.2. Preparation of the MnO_2-NiFe-LDH/CC Sample

First, 0.1 mmol of $KMnO_4$ was dissolved in 50 mL of deionized water under stirring at room temperature. The solution turned a clear purple-red after approximately 10 min. Then, the solution was transferred to a reactor and a piece of pre-treated NiFe-LDH/CC sample (2 × 3 cm^2) was added. The reactor was heated up to 120 °C and the temperature was maintained for 3 h. After the reaction, a brown precipitate was observed on the surface of the prepared catalytic sample. Subsequently, the sample was washed thoroughly with deionized water to remove any residual precipitate. Finally, the electrode sample was dried in a vacuum oven at 60 °C and labeled as MnO_2-NiFe-LDH/CC-0.1 mmol.

For comparative purposes, the amounts of $KMnO_4$ varied, at 0.05 mmol, 0.03 mmol, 0.01 mmol, 0.005 mmol, and 0.001 mmol under the same conditions. The obtained samples were labeled as MnO_2-NiFe-LDH/CC-0.05 mmol, MnO_2-NiFe-LDH/CC-0.03 mmol, MnO_2-NiFe-LDH/CC-0.01 mmol, MnO_2-NiFe-LDH/CC-0.005 mmol, and MnO_2-NiFe-LDH/CC-0.01 mmol, respectively.

4. Conclusions

In this work, a MnO_2-NiFe-LDH/CC electrode sample was prepared to investigate its oxygen evolution reaction (OER) catalytic performance and oxygen evolution selectivity in natural seawater. In the alkaline seawater electrolyte, the optimized MnO_2-NiFe-LDH/CC-0.01 mmol electrode sample exhibited overpotentials of 284 mV and 363 mV at current densities of 10 $mA \cdot cm^{-2}$ and 100 $mA \cdot cm^{-2}$, respectively, with a Tafel slope of 68.6 $mV \cdot dec^{-1}$. Additionally, the OER catalytic performance of this sample showed no significant degradation after 120 h of electrochemical testing. In natural seawater, the MnO_2-NiFe-LDH/CC-0.01 mmol sample demonstrated an oxygen evolution selectivity of 61.1%, which is superior to that of the NiFe-LDH/CC sample. This indicates that MnO_2 modification enhances the oxygen evolution competitiveness of the electrode material in seawater electrolysis. The study reveals MnO_2's potential to improve the oxygen evolution efficiency of catalysts under natural seawater conditions.

Supplementary Materials: The following supporting information can be downloaded at: https://www.mdpi.com/article/10.3390/catal14080502/s1, Figure S1. Schematic illustration of the preparation of the MnO_2-NiFe-LDH/CC sample; Figure S2. (a) OER LSV of the different loads of the MnO_2-NiFe-LDH/CC electrodes in alkaline seawater at a scan rate of 5 mV/s, (b) OER overpotential values at of 10 and 100 $mA \cdot cm^{-2}$, and (c) Tafel plots; Figure S3. SEM image of the CC substrate; Figure S4. (a–c) TEM images and (i) element mapping of the NiFe-LDH/CC sample; Figure S5. (a) Survey XPS spectrum of the NiFe-LDH/CC sample, with the deconvoluted high-resolution XPS spectra of (b) Ni 2p and (c) Fe 2p; Figure S6. (a) Survey of the XPS spectrum and (b) atomic percentage in the MnO_2-NiFe-LDH/CC-0.01 mmol sample; Figure S7. (a) OER LSV images for the CC, MnO_2/CC, NiFe-LDH/CC, and MnO_2-NiFe-LDH/CC-0.01 mmol electrode samples in alkaline seawater at a scan rate of 5 mV/s. (b) OER overpotential values of 50 and 100 $mA \cdot cm^{-2}$. (c) Tafel plots. (d) EIS spectra of CC, MnO_2/CC, NiFe-LDH/CC, and MnO_2-NiFe-LDH/CC-0.01 mmol samples. (e) Long-term chronopotentiometry of MnO_2-NiFe-LDH/CC-0.01 mmol samples under 10 mA·cm-2 for 100 h. (f) OER LSVs of the 1st and 6000th cycle on the MnO_2-NiFe-LDH/CC-0.01 mmol sample in alkaline seawater at a scan rate of 5. mV/s; Figure S8. CV curves at different scan rates in the alkaline seawater solution of the samples: (a) CC, (b) MnO_2/CC, (c) MnO_2-NiFe-LDH/CC-0.01 mmol, and (d) MnO_2-NiFe-LDH/CC-0.01 mmol and other catalysts; Figure S9. (a–e) Corresponding color changes during the titration. (f) State changes of the anode and cathode during constant current electrolysis. (g) The device that absorbs the chlorine gas; Figure S10. The schematic diagram illustrates the underlying synergetic effects and catalytic mechanisms of the NiFe-LDH/CC and MnO_2-NiFe-LDH/CC samples.

Author Contributions: F.L.: Conceptualization, Formal analysis, Investigation, Methodology, Writing-original draft, Visualization. M.F.: Methodology, Investigation, Writing-review & editing, Data curation. H.Y.: Methodology, Investigation. Z.W.: Literature search, make charts. J.R.: Writing-review & editing, Funding acquisition. J.S.: Resources, Project Administration. H.W.: Resources, Writing-review & editing, Supervision, Project Administration, Funding acquisition. All authors have read and agreed to the published version of the manuscript.

Funding: The authors thank the financial supports from the Natural Science Foundation of Shandong Province of China (ZR2022MB118) toward this research work.

Data Availability Statement: The data that support the findings of this study have been included in the main text and Supplementary Information. All other relevant data supporting the findings of this study are available from the corresponding authors upon request.

Conflicts of Interest: The authors declare no conflict of interest.

References

1. Yu, J.; Li, Z.; Liu, T.; Zhao, S.; Guan, D.; Chen, D.; Shao, Z.; Ni, M. Morphology control and electronic tailoring of CoxAy (A = P, S, Se) electrocatalysts for water splitting. *Chem. Eng. J.* **2023**, *460*, 141674–141701. [CrossRef]
2. Jiang, S.; Liu, Y.; Qiu, H.; Su, C.; Shao, Z. High selectivity electrocatalysts for oxygen evolution reaction and anti-chlorine corrosion strategies in seawater splitting. *Catalysts* **2022**, *12*, 261. [CrossRef]
3. Jiang, S.; Suo, H.; Zhang, T.; Liao, C.; Wang, Y.; Zhao, Q.; Lai, W. Recent advances in seawater electrolysis. *Catalysts* **2022**, *12*, 123. [CrossRef]

4. Sha, Q.; Shen, J.; Yang, G.; Li, T.; Liu, W.; Kuang, Y.; Sun, X. A single-atom Au catalyst boosts high-efficiency electrochemical seawater oxidation. *Catalysts* **2024**, *14*, 348. [CrossRef]
5. Lei, F.; Ma, X.; Shao, X.; Fang, Z.; Wang, Y.; Hao, W. Reasonable regulation of flexible sulfur-based bifunctional catalytic electrodes for efficient seawater splitting. *Inorg. Chem. Front.* **2024**, *11*, 2152–2163. [CrossRef]
6. Khan, I. Pluronic-123 Assisted synthesis of cobalt vanadate microparticles (μ-CoV MPs) for durable electrochemical oxygen evolution reaction in seawater and connate water. *Catalysts* **2023**, *13*, 636. [CrossRef]
7. Xu, L.; Dong, Y.; Xu, W.; Zhang, W. Ultrafast and facile synthesis of (Ni/Fe/Mo)OOH on Ni foam for oxygen evolution reaction in seawater electrolysis. *Catalysts* **2023**, *13*, 924. [CrossRef]
8. Das, D.; Santra, S.; Nanda, K.K. In Situ fabrication of a nickel/molybdenum carbide-anchored N-doped graphene/CNT hybrid: An efficient (Pre)catalyst for OER and HER. *ACS Appl. Mater. Interfaces* **2018**, *10*, 35025–35038. [CrossRef] [PubMed]
9. Xin, Y.; Hua, Q.; Li, C.; Zhu, H.; Gao, L.; Ren, X.; Yang, P.; Liu, A. Enhancing electrochemical performance and corrosion resistance of nickel-based catalysts in seawater electrolysis: Focusing on OER and HER. *J. Mater. Chem. A* **2024**. [CrossRef]
10. 46th ESAO Congress 3–7 September 2019 Hannover, Germany Abstracts. *Int. J. Artif. Organs* **2019**, *42*, 386–474. [CrossRef]
11. Wu, H.; Zhao, Z.; Wang, M.; Zheng, W.; Zhang, Y.; Wang, Y.; Ma, T.; Zeng, Z.; Cheng, C.; Li, S. Alkaline-earth-metal regulated metal carbides with bioinspired gradient OH spillover for efficient and long-lasting direct seawater electrolysis. *J. Mater. Chem. A* **2024**, *12*, 10755–10763. [CrossRef]
12. Abdul Razzaq, A.; Chen, G.; Zhao, X.; Yuan, X.; Hu, J.; Li, Z.; Chen, Y.; Xu, J.; Shah, R.; Zhong, J.; et al. Cobalt coordination with pyridines in sulfurized polyacrylonitrile cathodes to form conductive pathways and catalytic M-N4S sites for accelerated Li-S kinetics. *J. Energy Chem.* **2021**, *61*, 170–178. [CrossRef]
13. Wang, C.; Humayun, M.; Debecker, D.P.; Wu, Y. Electrocatalytic water oxidation with layered double hydroxides confining single atoms. *Coord. Chem. Rev.* **2023**, *478*, 214973. [CrossRef]
14. Liu, Y.; Lei, X.Y.; Xiong, B.; Chen, J.F.; Zou, W.; Fu, Z.P.; Lu, Y.L. Exploring the mechanism of the excellent catalytic activity of NiFe-layered double hydroxides in oxygen evolution reactions by modifying the iron content. *J. Chem. Res.* **2022**, *46*, 17475198221103519. [CrossRef]
15. Peng, L.S.; Yang, N.; Yang, Y.Q.; Wang, Q.; Xie, X.Y.; Sun-Waterhouse, D.; Shang, L.; Zhang, T.R.; Waterhouse, G.I.N. Atomic cation-vacancy engineering of NiFe-layered double hydroxides for improved activity and stability towards the oxygen evolution reaction. *Angew. Chem. Int. Ed.* **2021**, *60*, 24612–24619. [CrossRef] [PubMed]
16. An, X.Y.; Hu, Q.B.; Zhu, W.L.; Liu, L.N.; Zhang, Y.S.; Zhao, J.G. Partially amorphous NiFe-based bimetallic hydroxide nanocatalyst for efficient oxygen evolution reaction. *Appl. Phys. A-Mater. Sci. Process.* **2021**, *127*, 865. [CrossRef]
17. Liu, J.; Zhou, J.; Liu, S.; Chen, G.; Wu, W.; Li, Y.; Jin, P.J.; Xu, C.L. Amorphous NiFe-layered double hydroxides nanosheets for oxygen evolution reaction. *Electrochim. Acta* **2020**, *356*, 136827. [CrossRef]
18. Wei, H.S.; Liu, J.; Deng, Y.D.; Hu, W.B.; Zhong, C. Studies on the effect of the substrate on the electrocatalytic performance of electrodeposited NiFe hydroxides for oxygen evolution reaction. *Int. J. Electrochem. Sci.* **2019**, *14*, 4173–4184. [CrossRef]
19. Park, K.R.; Jeon, J.; Choi, H.; Lee, J.; Lim, D.H.; Oh, N.; Han, H.; Ahn, C.; Kim, B.; Mhin, S. NiFe layered double hydroxide electrocatalysts for an efficient oxygen evolution reaction. *ACS Appl. Energy Mater.* **2022**, *5*, 8592–8600. [CrossRef]
20. Dionigi, F.; Reier, T.; Pawolek, Z.; Gliech, M.; Strasser, P. Design criteria, operating conditions, and nickel–iron hydroxide catalyst materials for selective seawater electrolysis. *ChemSusChem* **2016**, *9*, 962–972. [CrossRef]
21. Chen, X.; Yu, Y.; Han, X.; Wang, H.; Hua, Y.; Wu, D.; Deng, P.; Xiao, J.; Tian, X.; Li, J. Introducing sulfur to nickel-iron selenide for high-efficiency alkaline seawater electrolysis. *Sci. China Chem.* **2024**, *67*, 2747–2754. [CrossRef]
22. Tang, M.; Du, K.; Yu, R.; Shi, H.; Wang, P.; Guo, Y.; Wei, Q.; Yin, H.; Wang, D. Microzone-acidification-driven degradation mechanism of the NiFe-based anode in seawater electrolysis. *ACS Appl. Mater. Interfaces* **2024**, *16*, 3260–3269. [CrossRef] [PubMed]
23. Chen, J.; Zhang, L.; Li, J.; He, X.; Zheng, Y.; Sun, S.; Fang, X.; Zheng, D.; Luo, Y.; Wang, Y.; et al. High-efficiency overall alkaline seawater splitting: Using a nickel–iron sulfide nanosheet array as a bifunctional electrocatalyst. *J. Mater. Chem. A* **2023**, *11*, 1116–1122. [CrossRef]
24. Sang, S.L.; Meng, H.M.; Shi, Y.H.; Yu, H.Y.; Fan, Z.S.; Sun, D.B. Preparation of oxygen evolution anodes for seawater electrolysis. In Proceedings of the 7th National Surface Engineering Academic Conference and the 2nd Surface Engineering Youth Academic Forum, Wuhan, China, 27–30 April 2015.
25. Vos, J.G.; Wezendonk, T.A.; Jeremiasse, A.W.; Koper, M.T.M. MnOx/IrOx as selective oxygen evolution electrocatalyst in acidic chloride solution. *J. Am. Chem. Soc.* **2018**, *140*, 10270–10281. [CrossRef]
26. Yan, H.; Wang, X.; Linkov, V.; Ji, S.; Wang, R. Selectivity of oxygen evolution reaction on carbon cloth-supported delta-MnO_2 nanosheets in electrolysis of real seawater. *Molecules* **2023**, *28*, 854. [CrossRef]
27. Chang, J.; Zang, S.; Song, F.; Wang, W.; Wu, D.; Xu, F.; Jiang, K.; Gao, Z. Heterostructured nickel, iron sulfide@nitrogen, sulfur co-doped carbon hybrid with efficient interfacial charge redistribution as bifunctional catalyst for water electrolysis. *Appl. Catal. A Gen.* **2022**, *630*, 118459–118468. [CrossRef]
28. Ganesan, P.; Sivanantham, A.; Shanmugam, S. Inexpensive electrochemical synthesis of nickel iron sulphides on nickel foam: Super active and ultra-durable electrocatalysts for alkaline electrolyte membrane water electrolysis. *J. Mater. Chem. A* **2016**, *4*, 16394–16402. [CrossRef]
29. Han, C.; Li, W.; Shu, C.; Guo, H.; Liu, H.; Dou, S.; Wang, J. Catalytic activity boosting of nickel sulfide toward oxygen evolution reaction via confined overdoping engineering. *ACS Appl. Energy Mater.* **2019**, *2*, 5363–5372. [CrossRef]

30. Han, Y.; Zeng, X.; Liu, Y.; Shi, S.; Xiong, P.; Wang, T.; Pan, X.; Li, J.; Hu, W.; Deng, Y. Crystalline–amorphous Ni4.5Fe4.5S8/NiFeS heterostructure for alkaline water oxidation electrocatalysis. *Mater. Today Energy* **2023**, *38*, 101442–101450. [CrossRef]
31. Xu, W.; Zhang, J.-P.; Tang, X.-Q.; Yang, X.; Han, Y.-W.; Lan, M.-J.; Tang, X.; Shen, Y. Highly efficient sulfur-doped Ni3Fe electrocatalysts for overall water splitting: Rapid synthesis, mechanism and driven by sustainable energy. *J. Colloid Interface Sci.* **2024**, *653*, 1423–1431. [CrossRef]
32. Zhang, M.; Chang, S.; Chen, X.; Zhang, Y.; Zhang, Z.; Xue, H.; Deng, Y.; Jiang, Y. Regulating electron-spin state enables enhanced electrocatalytic water splitting properties in bimetallic sulfides. *Fuel* **2024**, *362*, 130941–130950. [CrossRef]
33. Meng, X.-y.; Wang, M.; Zhang, Y.; Li, Z.; Ding, X.; Zhang, W.; Li, C.; Li, Z. Superimposed OER and UOR performances by the interaction of each component in an Fe–Mn electrocatalyst. *Dalton Trans.* **2022**, *51*, 16605–16611. [CrossRef] [PubMed]
34. Fan, H.; Ma, Y.; Chen, W.; Tang, Y.; Li, L.; Wang, J. Facile one-step electrodeposition of two-dimensional nickel-iron bimetallic sulfides for efficient electrocatalytic oxygen evolution. *J. Alloys Compd.* **2022**, *894*, 162533–162541. [CrossRef]
35. Choi, D.; Ryu, S. Efficient and selective oxygen evolution reaction in seawater electrolysis with electrochemically synthesized amorphous-like NiFes. *Electron. Mater. Lett.* **2023**, *20*, 173–182. [CrossRef]
36. Han, Y.; Shao, L.; Liu, Y.; Li, G.; Wang, T.; Zheng, X.; Li, J.; Han, X.; Hu, W.; Deng, Y. Sulfate-assisted Ni/Fe-based electrodes for anion exchange membrane saline splitting. *Nano Res.* **2024**, *17*, 5985–5995. [CrossRef]
37. Jeung, Y.; Roh, H.; Yong, K. Co-anion exchange prepared 2D structure Ni(Co,Fe)PS for efficient overall water electrolysis. *Appl. Surf. Sci.* **2022**, *576*, 151720–151727. [CrossRef]